energies

MDPI

Article

Roadway Embedded Smart Illumination Charging System for Electric Vehicles

Daniel Fernandez [1], Ann Sebastian [1], Patience Raby [2], Moneeb Genedy [2], Ethan C. Ahn [1], Mahmoud M. Reda Taha [2], Samer Dessouky [3] and Sara Ahmed [1,*]

[1] Department of Electrical and Computer Engineering, University of Texas at San Antonio, 1 UTSA Circle San Antonio, San Antonio, TX 78249, USA
[2] Department of Civil, Construction and Environmental Engineering, University of New Mexico, Albuquerque, NM 87131, USA
[3] School of Civil and Environmental Engineering and Construction Management, University of Texas at San Antonio, 1 UTSA Circle San Antonio, San Antonio, TX 78249, USA
* Correspondence: sara.ahmed@utsa.edu

Abstract: Inspired by the fact that there is an immense amount of renewable energy sources available on the roadways, such as mechanical pressure, this study presents the development and implementation of an innovative charging technique for electric vehicles (EVs) by fully utilizing the existing roadways and state-of-the-art nanotechnology and power electronics. The developed Smart Illuminative Charging is a novel wireless charging system that uses LEDs powered by piezoelectric materials as the energy transmitter source and thin film solar panels placed at the bottom of the EVs as the receiver, which is then poised to deliver the harvested energy to the vehicle's battery. The piezoelectric materials were tested for their mechanical-to-electrical energy conversion capabilities and the relatively large-area EH2N samples (2 cm × 2 cm) produced high output voltages of up to 52 mV upon mechanical pressure. Furthermore, a lab-scale prototype device was developed to testify the proposed mechanism of illuminative charging (i.e., "light" coupled pavement and vehicle as a wireless energy transfer medium).

Keywords: wireless charging; electric vehicles; piezoelectric effect; LEDs; solar panels

Citation: Fernandez, D.; Sebastian, A.; Raby, P.; Genedy, M.; Ahn, E.C.; Taha, M.M.R.; Dessouky, S.; Ahmed, S. Roadway Embedded Smart Illumination Charging System for Electric Vehicles. *Energies* **2023**, *16*, 835. https://doi.org/10.3390/en16020835

Academic Editors: Ayman S. Mosallam, Haohui Xin, Brahim ELBHIRI, Shaohua He and Shadi M. Saadeh

Received: 9 November 2022
Revised: 22 December 2022
Accepted: 25 December 2022
Published: 11 January 2023

1. Introduction

Roadways are an important part of transportation infrastructure, serving as a backbone to enable better mobility for people and goods. Because the roadways greatly impact the economic growth and development of the communities, state-of-the-art research has focused on planning, designing, and constructing roadways to reduce environmental impact, increase sustainability, and improve the efficiency of transport flow [1,2]. However, due to increasingly large demands for reduced driver stress, independent mobility for non-drivers, and increased safety, further research is called for on the development of novel roadways that can adapt for future vehicles (e.g., electric, or self-driving vehicles).

Electric vehicles (EVs) are promoted as a key contributor to building this sustainable mobility system [3]. They are generally much more energy efficient than gas-powered vehicles. Increasing the use of EVs can result in considerably lower emissions of carbon dioxide and other air pollutants, including nitrogen oxides and particulate matter (PM), and therefore decrease the air quality problems and preserve the environment [4]. However, the adoption of EVs could lead to overloading the grid and degrading the power quality of the distribution system. It also demands an increase in the number of EV charging stations. To meet the EV charging needs of 15 million EVs by the year 2030, with limited charging stations [5,6], prediction of charging needs and reallocating charging resources are emerging needs, especially due to the coincidence between utility peak power loading and EV charging [7]. Multiple studies proposed different optimization and stochastic

planning models that utilize the limited network resources with the increase in uncertain distribution generation, such as renewables and EVs [8,9]. In [10], the authors focused on the impacts of EVs on the electricity generation, and in [11], the authors proposed investment in operation models of Grid-to-Vehicle (G2V), Vehicle-to-Grid (V2G), and Vehicle-to-Building (V2B) for the large-scale and long-term network expansion planning problems under multi-dimensional uncertainty.

In addition, these EVs need to be equipped with a large-capacity battery pack as an energy storage unit to operate for a satisfactory distance [12,13]. Lithium-ion batteries, the most commonly used battery in today's EVs, have an energy density of only 90–100 Wh/kg [14,15], which is very low when compared with that of gasoline (about 12,000 Wh/kg). Therefore, lithium-ion battery operated EVs can only operate for about a 300-mile range, and then they need to be recharged [16,17]. In addition to the low energy density, contemporary battery technologies have thee shortcomings of long charging time, large size and weight, limited lifetime, and high cost. To overcome these challenges, alternative charging strategies that utilize renewable energy sources and roadways need to be developed. Currently, the stationary charging systems of EVs fall under three categories: Level 1, 2, and 3 charging stations. Level 1 charging stations use a 120 VAC plug supplying 3–5 miles per hour using a standard outlet. Level 2 EV charging stations are used for both residential and commercial charging stations. They use a 240 V (for residential) or 208 V (for commercial) plug, charging at a rate of 10–20 miles per hour. Level 3 charging stations, also known as DC fast chargers, use a 208 V (for commercial) plug or are connected to a 480 V 3-Phase AC source, and can charge 80 percent of an EVs battery in 20–30 min [18]. Alternatives to stationary charging stations have also been introduced, for example, wireless power transfer (WPT) charging [19], and photovoltaic (solar) vehicles [20]. Wireless power transfer (WPT) for EVs has been introduced by using magnetic resonance to create a field between a ground charging coil and a copper coil embedded in a vehicle. A research team from MIT first demonstrated in 2007 that 60 watts of power can be transferred at a 2 m distance according to the coupled magnetic resonance theory [21]. Many researchers followed this groundbreaking work on wireless power transfer (WPT) mechanisms, suggesting innovative circuits and performing system-level analysis with improved control [22–27]. The WPT system uses ferrite as a magnetic flux guide and aluminum plate as a shield to generate a resonance frequency of a maximum of 100 kHz [28]. Multiple other works on WPT systems for EV charging include the online electric vehicle (OLEV), designed by the Korea Advanced Institute of Science and Technology (KAIST), with its three generations of a light golf cart, a bus (60 kW power transfer with efficiency of 70%), and an SUV (20 kW with efficiency of 83%) [29,30], and the Oak Ridge National Laboratory (ORNL)'s wireless charging system prototype for an EV with efficiency of nearly 90% for 3 kW power delivery [31]. Recent work by the University of Michigan, Dearborn, also attracted much attention due to a 200 mm distance, 8 kW WPT system, which achieved efficiency as high as 95.7% [32]. Despite the popularity and maturity of the WPT technology for EV charging, its relatively high cost and limited distance for power transmission (maximum of 3 ft) still remains a great challenge. Solar power is another method for charging EVs wirelessly without entirely relying on batteries, as energy can be harnessed from the sun and converted into electricity by placing solar panels on a vehicle's roof. For example, a solar vehicle company, Lightyear, recently emerged with the promise of delivering practical solar-powered vehicles by 2030 [33], and a Chinese solar panel manufacturer, Hanergy Holding group, formed a Solar Vehicle Business Division with four PV prototypes for solar-powered vehicles [33]. However, this type of charging solution is only feasible when sunlight is available (e.g., during the daytime); the vehicle batteries should still be charged using power from the grid during nighttime. Moreover, solar-powered EVs are still not mature enough to be economically available to customers, largely due to multiple technical and manufacturing challenges in the contemporary PV cell technology, such as the engineering tradeoff between cost and energy conversion efficiency.

There are many applications of harvesting energy using the roadway, due to multiple renewable energy sources available through roadways: optical (light), thermal (heat), and mechanical (deformation or friction) energies. One form of energy harvesting is solar pavement, a form of pavement that generates electricity by collecting solar power with photovoltaic cells [34], and is installed in various roadway infrastructures. The solar pavement panels consist of three (3) layers: (1) The road surface has PV cells which collect the sunlight; (2) The electronic layer contains a mini microprocessor board that helps control the heating element of the panels (e.g., this heating capability can help melt the snow that lands on the panels); and finally, (3) The base plate layer collects the energy from the sun and distributes the power [35]. Another form of energy harvesting is Asphalt Solar Collectors (ASCs); ASCs use asphalt and tarmac to absorb the sun's rays and heat water for domestic use [36]. ASCs consist of pipes embedded in the pavement with a circulating fluid inside. Due to the temperature gradient between the fluid circulating through pipes and the pavement [37], a heat transfer occurs from the pavement to the fluid, which leads to a temperature drop in pavement and a temperature increase in fluid, creating energy. Recent research studies have considered the potential of functional (e.g., piezoelectric or thermoelectric) nanomaterials to generate electricity from mechanical pressure or frictional heat. The reasoning behind this nanomaterials-based energy harvesting system is that the nanomaterial can be embedded inside the roadway pavement or the vehicle tire [38,39] such that the mechanical or thermal excitation is induced in the nanomaterial by tire loading of the vehicles, producing separation of electrical charges. Although the voltage and power level generated from this nano-generator system may be relatively low, this approach has great potential to advance the energy harvesting technology by miniaturizing the system and facilitating its integration with other existing infrastructures.

The primary objective of this study is to introduce an innovative Smart Illuminative Charging (SIC) method for EVs by using renewable energy sources available on roadways, such as mechanical pressure and frictional heat. This study introduces a novel wireless power system where (a) nanomaterials-powered light-emitting diodes (LEDs), as the energy transmitter, are embedded under a transparent polymer modified nanocomposite (TPMN) overlay and (b) thin-film photovoltaic (PV) solar panels, as the energy receiver, are placed under each vehicle (See Figure 1). The energy harvested during vehicle motion by using cutting-edge low-dimensional nanomaterials are transferred to the vehicle's main power supply, i.e., the battery. The study will also discuss a lab-scale proof-of-concept prototype for a smart charging system for vehicles. The prototype represents the integration of existing roadways, state-of-the-art nanomaterials, and power electronics technologies to create a smart, sustainable transportation infrastructure.

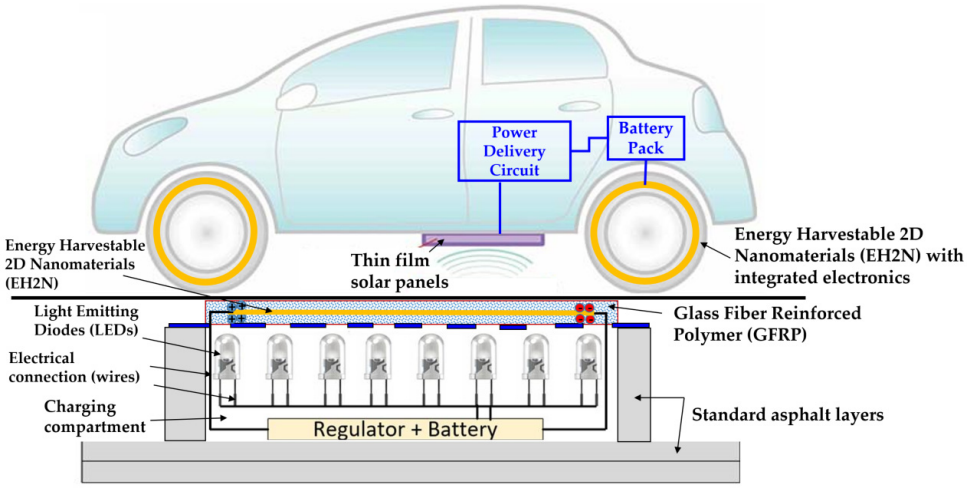

Figure 1. Schematic of the smart charging system proposed for EVs and roadway infrastructure.

2. Methods

The SIC system developed in this study features the following three sequential pathways of energy conversion: (1) the mechanical energy available on the roadway is converted into electrical energy through the use of energy-harvestable 2D nanomaterials (EH2N) (See Figure 2a), (2) the harvested energy is used (instead of the conventional power grid) to power the LEDs embedded in the roadway, and (3) the PV panels attached to the vehicle bottom finally convert the received light energy back to electricity. In the following sections, the components of the system as shown in Figure 1 will be discussed in detail.

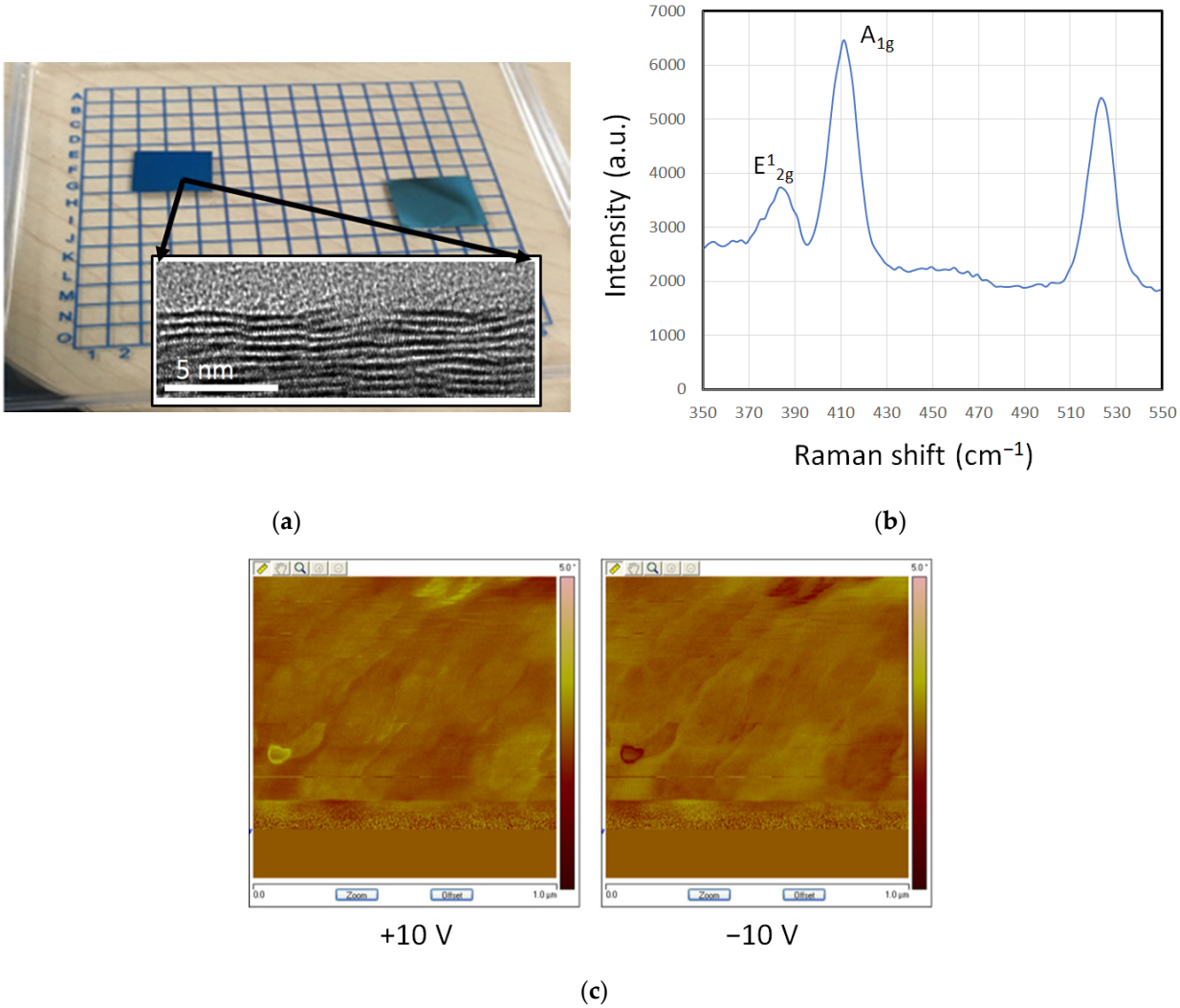

Figure 2. EH2N testing (**a**) EH2N grown by CVD (**b**) Raman characterization data of EH2N grown on a SiO_2/Si substrate (**c**) PFM measurements of EH2N. The observed phase shift between the two different voltage polarities indicate that the EH2N thin film expands and contracts with the electric field direction (i.e., piezoelectric).

2.1. Photovoltaic Solar System

There are various solar panels based on semiconductor materials and manufacturing methods. The types of solar panels that can be found on the market, based on the materials and manufactured process, are: (1) monocrystalline panels, (2) polycrystalline panels, (3) amorphous panels, and (4) tandem panels. Monocrystalline panels are called first generation, and are made of sections of a silicon bar in one piece, crystallized perfectly. The efficiency of these panels does not reach more than 24.7% in laboratory and 16% for commercial ones. The polycrystalline panels are similar to the previous type, but, in this case, the process of silicon crystallization is different. Polycrystalline panels are

formed by pieces of a silicon bar that have been structured as disordered crystals. They are visually very recognizable because they present a granulated surface. A lower efficiency than mono crystalline (19.8% laboratory, and commercial modules, 14%) is provided by these panel, and, consequently, the price is lower. Amorphous panels have a considerable thickness. Using silicon with another structure or other semiconductor materials, thinner and versatile panels can be obtained. Amorphous PV Solar Panels or thin-film PV modules, the second-generation panels, are classified according to the material employed. Unlike the previous generation, amorphous panels do not have a crystal structure. Panels of this type are commonly used for small electronic devices (calculators, watches) and small portable panels. Its peak performance in the laboratory is about 13%, and 8% in the commercial modules. Other examples are cadmium telluride, with a performance in laboratory of 16% and 8% in commercial modules, and gallium arsenide, one of the most efficient materials, with 20% efficiency on commercial panels [40,41]. These second-generation cells are more flexible, cheaper, take up less physical space, and are less impacted by high temperatures and shading, but they degrade faster and have lower efficiency than that of the first generation. Finally, there are also tandem panels, which combine two different types of semiconductor materials [42,43]. Each type of material absorbs only a part of the electromagnetic spectrum of solar radiation, and, because of this, a combination of two or three types of materials can be used to collect more than one of the electromagnetic spectrums. This type of panel can be as efficient as 35%. There is also a third generation of panels, that are "emerging photovoltaics"; most are still in the prototype phase and not commercially available.

In Table 1, six solar panels from five companies were considered. The criteria used to choose the solar panels were the power rating and the cost. The cost for the second generation relative to the power generated made the first generation solar panels more competitive. The big disadvantage of first generation in our application is the rigidness of the solar panels. This was counteracted by the monocrystalline solar cells encased in ethylene vinyl acetate, ethylene tetrafluoroethylene, and tedlar polyester tedlar, which is the combination of using both the first generation solar cells and the second generation solar cells flexibility. This results in the most efficient and flexible solar cell that facilitates easier integration in our proposed charging system.

Table 1. Analysis of solar panels in the current market.

Manufactuerer	Power Rating	V_{mp}	I_{op}	Price	Generation
EcoWorthy®	10 W	17.3 V	0.58 A	$21.16	First
Renogy®	30 W	17.5 V	1.71 A	$59.99	First
SunKingdom®	13 W	12.0 V	1.08 A	$33.99	First + Second
Zerodis®	4.5 W	18.0 V	0.25 A	$29.99	Second
EcoWorthy®	5.0 W	17.9 V	0.28 A	$20.73	Second
Lensun®	20 W	18.0 V	1.11 A	$79.00	First + Second

2.2. Light Emitting Diodes (LEDs)

A light emitting diode (LED) is a semiconductor light source that emits light when current flows through it. LEDs have many advantages over incandescent light sources, including lower energy consumption, longer lifetime, improved physical robustness, smaller size, and faster switching. The major criterion for choosing LEDs is their conversion measured as Lumens per Watt (lm/W) and flexibility. LEDs emit more lumens per watt than incandescent light bulbs [44]. LEDs can have a relatively long useful life [45,46]. Several Department of Energy (DOE) demonstrations [47] have shown that the reduced maintenance cost from this extended lifetime, rather than energy savings, is the primary factor in determining the payback period for an LED product. There are four types of LEDs: Miniature LEDs, Red–Green–Blue (RGB) LEDs, LED strips, and LED tubes. Based on the

current market availability, approximately 200 lm/W is the maximum expected output, so we implemented Samsung Semiconductor Inc. LM561C LEDs [48].

2.3. Energy-Harvestable 2D Nanomaterials

Two-dimensional (2D) nanomaterials [49] are an emerging class of materials, with properties making them highly attractive for both fundamental exploration of physical phenomena and practical engineering applications across a variety of disciplines, including energy harvesting. These 2D nanomaterials exhibit a unique, unmatched portfolio of functionalities and capabilities beyond the conventional materials at the fundamental scaling limit (thicknesses of a few nanometers), and favorable electronic, mechanical, and optical properties. For the purpose of this study, their promising piezoelectric (energy harvesting) properties with excellent flexibility and transparency are of particular interest. Unlike most of the previous studies [50,51], which used 2D nanomaterial flakes, this study features the chemical vapor deposition (CVD)-based large-area material preparation. The area of otherwise "exfoliated" 2D nanomaterial flakes is limited to hundreds of micrometers squared, thus limiting their adoption in large-area integration such as in the proposed SIC system for EVs. The CVD process is more scalable, in that growth is only limited by the CVD system itself. In this study, the high-quality, large-area (up to 2 cm × 2 cm) EH2N was prepared and characterized for the novel purpose of using them as a scalable, mechanically robust energy harvesting source that can be integrated in the existing roadway infrastructure. The next subsection discusses the sample preparation and highlights its main structure and piezoelectric characteristics.

2.3.1. Sample Preparation

Two-dimensional nanomaterials were prepared utilizing the CVD technique [52] in "2 cm × 2 cm" square samples. The EH2N was successfully synthesized and deposited on the SiO_2/Si substrate in the quartz tube CVD furnace at a large scale using the method described in the literature [52]. The thickness of EH2N ranges from 1.5 to 2 nm, as confirmed in the cross-sectional transmission electron micrograph (TEM) image shown in Figure 2a. It is highlighted that a commercially available substrate material (SiO_2/Si) was used for nanomaterial synthesis, and the nanomaterial can be readily transferred to any other substrate.

2.3.2. Structural Characterization

The prepared EH2N material was studied using the Raman Spectroscopy technique, a well-established tool used to analyze a variety of low-dimensional nanomaterials, including graphene, carbon nanotubes, and transition metal dichalcogenides [53]. Figure 2b shows the measured Raman spectrum of as-grown EH2N layers on a SiO_2/Si substrate, indicating two distinct peaks corresponding to the in-plane ($E^1{}_{2g}$) and out-of-plane ($A^1{}_g$) lattice vibration modes. Combined with the other microscopic characterization techniques applied, this set of structural characterizations confirms that the EH2N thin film was prepared with no significant amount of crystalline defects and imperfections, which is critical to ensure its piezoelectric (energy harvesting) behavior.

2.3.3. Piezoelectric Characterization

The EH2N's piezoelectricity was experimentally characterized by adopting the piezo response force microcopy (PFM) technique. The PFM is a well-established approach for probing piezoelectric properties at the nanoscale. Based on the coupling between polarization and mechanical displacement, a highly localized electric field is applied to the material and then the resultant surface displacement is measured. The following equations provide an elementary theory of the PFM measurement.

$$V_{tip} = V_{dc} + V_{ac} \cos \omega t \tag{1}$$

$$A = A_0 + A_1 \omega \cos(\omega t + p) \tag{2}$$

where V_{tip} is the voltage applied to the conductive tip, V_{dc} is the DC voltage bias (switching bias), V_{ac} is the AC voltage bias (probing bias), and ω = the driving frequency of the AC bias.

As the sample expands or contracts due to the inverse piezoelectric effect, the tip deflection can be monitored using a lock-in amplifier because the tip oscillation (A) will have the phase shift (p) between the driving voltage (V_{ac}) and the voltage-induced mechanical deformation ($A_{1\omega}$), as well as the static surface displacement (A_0). When the polarization and applied electric field were parallel (Figure 2c left subpanel, +10 V), the deformation was positive (i.e., expansion) and the PFM signal was in phase with V_{ac}. On the contrary, when the opposite electric field (Figure 2c right subpanel, −10 V) was applied, this caused the EH2N to contract with the consequent lowering of the PFM cantilever tip. This led to the 180° phase shift, as seen in the right subpanel. Given that all materials that exhibit this so-called inverse piezoelectric effect are essentially piezoelectric, this measurement proves that the prepared nanomaterial (EH2N) is a strong piezoelectric material that can be harnessed for the energy harvesting or mechanical-to-electrical energy conversion purpose.

2.4. Fabrication and Testing of Electrically Conductive Glass Fiber Reinforced Polymer

A new glass fiber reinforced polymer (GFRP) composite overlay incorporating nanomaterials was developed with improved mechanical properties and electrical conductivity. The new multi-function GFRP composite can be connected to electrical power generating materials and conduct electricity to illuminate the LEDs. The new composite also has self-sensing ability, and can detect mechanical damage under loading by observing changes in its electrical conductivity.

To fabricate electrically conductive GFRP, epoxy-carbon nanofiber (CNFs) composite was first fabricated. The CNFs were supplied by Nanostructured and Amorphous Materials Inc. Their diameters vary from 80 to 200 nm and their lengths from 0.5 to 20 µm, and thus the aspect ratio ranges between 6.3 and 100. The epoxy used in fabrication was EPOTUF® 37-127, supplied by U.S. Composites, Inc. (Riviera Beach, FL, USA) [54]. The epoxy resin is a low viscosity, 100% reactive, diluted liquid based on Bisphenol-A containing glycidyl ether. The hardener was Aliphatic Amine EPOTUF® 37-614 [55]. The resin to hardener mixing ratio was 2:1. The bidirectional S-Glass fiber fabric was supplied by ACP Composites, Inc. The epoxy hardener was added to the resin-CNFs mixture to fabricate the GFRP using the vacuum assisted hand lay-up technique, following ASTM standard D5687. A stage for fabrication of GFRP was then built. This stage includes a metal plate fixed in place on the lay-up table. A non-porous release film was attached to isolate the GFRP panels from the metal plate. Peel ply was added over the non-porous release film to facilitate peeling of GFRP panels after epoxy curing. Afterwards, the glass fiber fabrics layers were placed on the peel ply. Each layer was impregnated in the epoxy using a roller, consuming approximately 45 gm of epoxy per layer. Another peel ply was applied over the GFRP layers, and then a porous release film was added. To provide an air bath to facilitate absorbing the excess epoxy, a breather ply layer was added over the porous release film. Finally, a nylon bag with an opening for the vacuum port was attached to a sealant tape over the metal plate to seal the entire system. Six layers of bidirectional plain weave glass fiber textile fabrics were laid in 0° direction, and then vacuum pressure was applied. A vacuum pump was connected to apply a vacuum pressure for 24 h to remove air bubbles and excess epoxy. After 24 h, the vacuum pump, nylon bag, and release films were removed. The GFRP composite plates were then cured for 2.5 days at 110 °C to ensure complete curing. The CNF content of 2.0 wt.%, used for producing the GFRP composites, was based on the electrical percolation observations of epoxy-CNFs nanocomposites discussed below. Figure 3 shows the vacuum hand lay-up technique used to fabricate the GFRP composites.

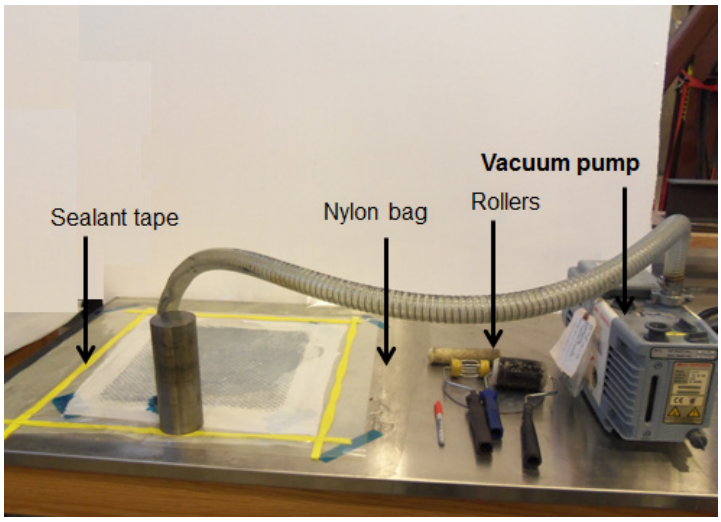

Figure 3. GFRP fabrication using vacuum hand lay-up technique.

Fiber volume fraction of GFRP composites incorporating 2.0 wt.% CNFs was found to be 55%, determined using ASTM D3171. A scanning Electron Microscope (SEM) using Quanta 250 was used to examine the dispersion of CNFs in epoxy. SEM images of CNFs in the epoxy matrix are shown in Figure 4. The images demonstrate the efficient dispersion of CNFs in the epoxy matrix prior to fabrication of GFRP.

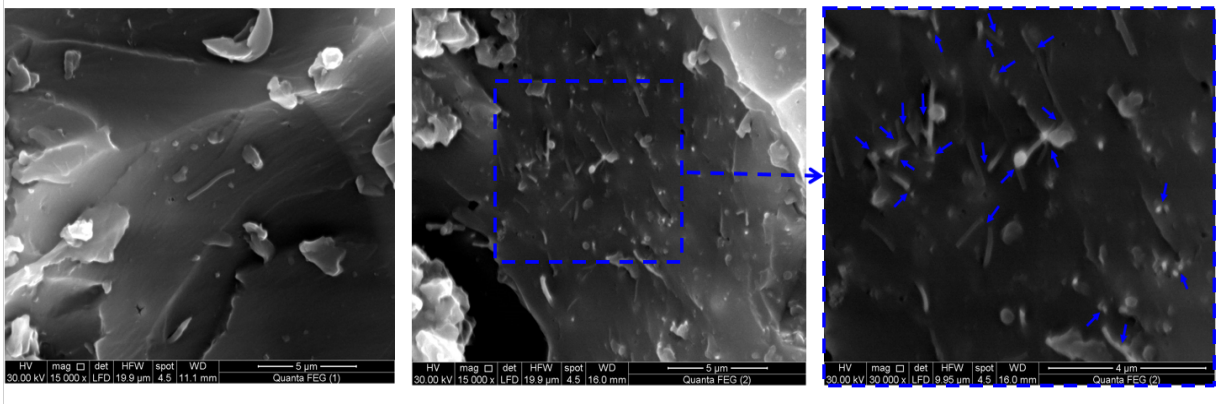

(**a**) (**b**) (**c**)

Figure 4. SEM images of CNFs in the epoxy matrix; (**a**) 0.5 wt.%; (**b**) 2.0 wt.%; and (**c**) a close view of 2.0 wt.% CNFS shows the formation of conductive network inside epoxy.

Five GFRP composite coupons of 19 mm × 150 mm were tested under off-axis (i.e., load was applied at 45° with respect to the fiber direction) static monotonically increasing tension stress. The static tension tests were performed using MTS® servo hydraulic machine [56]. A displacement control protocol was used in the static tension tests according to the ASTM standards methods D3039/D3039M, with a loading rate of 1.0 mm/min. The electrical resistance of the glass fiber composite specimens was measured during the tension test using a Keithley 2636B source meter. Conductive electrodes were applied to the glass fiber composite coupon using silver paint at two points spaced by 50 mm to allow electric resistance measurements. A schematic representation of the electrical resistance measurement during the static monotonically increasing tension test is shown In Figure 5.

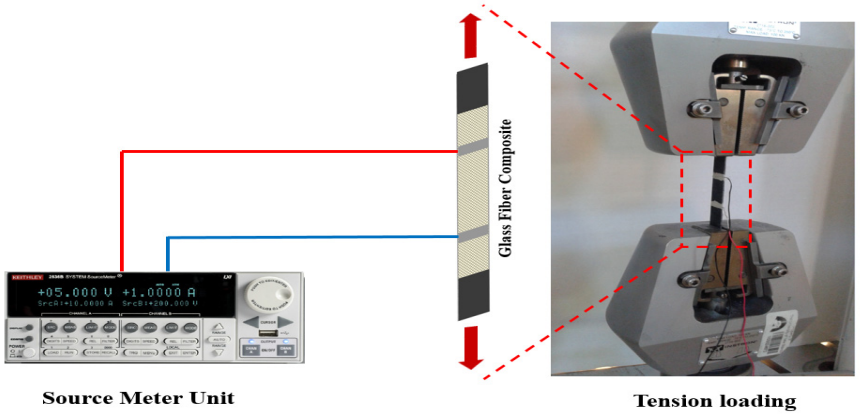

Figure 5. Schematic of electrical resistance measurement of glass fiber composite coupons during tension tests.

Damage in glass fiber composite coupons was estimated in terms of the change of the electrical conductivity during loading. The electrical conductivity was measured, and a metric of damage based on electrical conductivity change, denoted $D_E(t)$, was calculated using Equation (3):

$$D_E(t) = 1 - \frac{\sigma(t)}{\sigma(t_0)} \% \quad (3)$$

where $D_E(t)$ = the electrical damage measured at time t, $\sigma(t_0)$ = the initial electrical conductivity of the composite prior to load application at time t_0 and $\sigma(t)$ = the electrical conductivity of the composite at time t.

Moreover, a metric of damage based on change of modulus of elasticity, representing mechanical damage and denoted $D_M(t)$, was calculated using Equation (4):

$$D_M(t) = 1 - \frac{E(t)}{E(t_0)} \% \quad (4)$$

where $E(t_0)$ is the initial tangent modulus of elasticity of the glass fiber composite coupon at t_0 and $E(t)$ is the tangent modulus of elasticity of the glass fiber composite coupon at time t. A minimum tangent modulus of zero was assumed to account for the descending stress–strain.

2.5. Power Delivery Circuit Design

A power conditioning circuit that converts the received light energy in the PV panels back to electricity and charges a battery representing the vehicle battery was designed. A synchronous, switch-mode battery charge control was used to implement maximum power point tracking (MPPT). The MPPT is an algorithm utilized in charge controllers to extract the maximum power from a photo-voltaic (PV) module [57]. The voltage of a PV module at the maximum power is called the peak power voltage. To implement this, the bq24650EVM evaluation module [58] was used. The module takes a solar panel as the input, and the output as two loads. The first load is the system denoted by V_{sys}, which represents what will be powered (i.e., actuators, sensors, etc.), and the second load is the charger output denoted by V_{out},, which will be a 12-volt lead–acid battery. For the lab prototype, a resistive load is used to calculate the power output from V_{sys}. Utilizing the bq24650EVM evaluation module increases the efficiency of the PV array output, which is necessary to reduce all power losses within the system.

3. Lab-Scale Proof-of-Concept Design of the Proposed Smart Charging System

Figure 6 shows the lab-scale proof-of-concept prototype of the smart charging system designed and implemented in this study. The prototype consists of two 150 cm pieces of track with five 60 cm divisions (Figure 6 shows only half of the track); the divisions

alternate from wood to plexiglass, starting and ending with wood representing the asphalt, and the plexiglass divisions will represent compartments that will be embedded in the wheel paths on the embedded roadway.

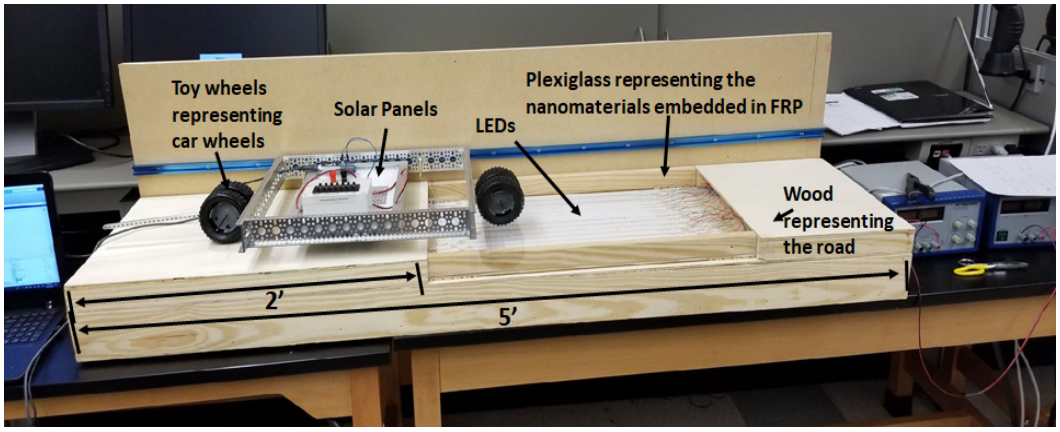

Figure 6. Lab scale proof-of-concept design of the prototype.

The LEDs are located under the transparent plexiglass, which simulates the portion of roadway pavements with EH2Ns embedded. The prototype used 16 LED strips under each plexiglass division, with ratings of 21.9 V and 450 mA per strip. The strips were connected in parallel to have a constant voltage. The LEDs strips are partially powered by a DC source in the prototype. However, given that the voltage per area obtained from nanomaterials is 130 V/m^2, a continuous nanomaterial film of the full area of the LED compartment (60 × 45 cm), will enable the lighting up of all LEDs using the 2D nanomaterial. Since the proposed 2D nanomaterials are still under development and not commercially available, fabricating a large continuous nanomaterial was beyond the scope of this study. On top of the plexiglass, solar panels are placed in a frame with wheels riding along a track to simulate the vehicle with the solar panel on its bottom. The prototype was used to test the viability of the proposed smart illuminative charging system.

3.1. Solar Panel Configuration

For the smart charging system prototype, three solar panels frames are utilized with power ratings ranging between 26 and 30 W, as shown in Figure 7. These three configurations use three of the solar panels chosen in Table 1. Two configurations use the standard first-generation mono-crystalline solar panels. The first solar configuration uses three 10 W EcoWorthy® panels, with an efficiency greater than 17%, in parallel to obtain 30 W. The second configuration also uses the standard first-generation configuration, but uses only one panel of the Renogy® 30 W monocrystalline solar panel, with a rated efficiency of 21%. The third solar panel configuration tested combines characteristics of the first and second-generation solar panels, thus being mono-crystalline and semi-flexible. This hybrid solar panel configuration uses two panels rated at 13 W from SunKingdom®, with a 23.5% efficiency.

Figure 7. Three solar panel frames constructed for lab-scale prototype: Top to bottom: Three 10 W EcoWorthy®, 30 W Renogy®, 2–13 W SunKingdom®.

3.2. MPPT Circuit for Solar Panels and Communication and Sensing Circuit for LEDs

Data logging was a key component in collecting results while the solar panels were stationary and in motion. There was a need for wireless data. To transfer data wirelessly, Bluetooth communication was employed. A master Bluetooth module (HC-05) [59] gathered and transmitted data from a voltage sensor connected to the solar panels, to a slave Bluetooth module (HC-06) connected to a laptop through a serial port. Data was then recorded in a terminal software program. Utilizing the data, the resulting waveforms are plotted in MATLAB [60].

An ultrasonic sensor connected to an Arduino was used for sensing if the solar panel configurations are passing over the plexiglass compartment. If the distance of the ping was shorter than the threshold that was set, the relay on the batteries would activate. A relay is an electrically operated switch, the JBtek 4 Channel DC 5 V Relay Module, consisting of four single pole single throw switches. The module was used because there are four arrays of eight LED strips within the prototype. This configuration allows for each LED array to have a separate power supply.

4. Performance Analysis and Findings

4.1. Harvested Voltage from EH2N

To further emulate the practical situation where the nanomaterial (embedded in roadways) is exposed to a significant amount of mechanical pressure, the EH2N sample's energy harvesting property was examined by bending it and directly measuring the induced output voltage (i.e., piezoelectrically induced polarization charges). For this experiment, the EH2N was transferred onto a flexible substrate (polyimide film) and the electrode was deposited on the sides by the e-beam evaporation and shadow mask techniques. As seen in Figure 8, the mechanically strained (by 0.5% to 1%) nanomaterial was able to produce an output voltage of up to 52 mV, which is higher than the state-of-the-art reported peak output of 15 mV and 20 pA [29]. Given that the voltage per area measured from

nanomaterials is 130 V/m^2, if we have a continuous nanomaterial film of the full area of the LED compartment in the prototype (2 ft × 1.5 ft), we will then be able to light up all the LEDs using the 2D nanomaterial, which shows promising results. This result proves the EH2N's potential to become an alternative energy source from the ground when embedded in roadways.

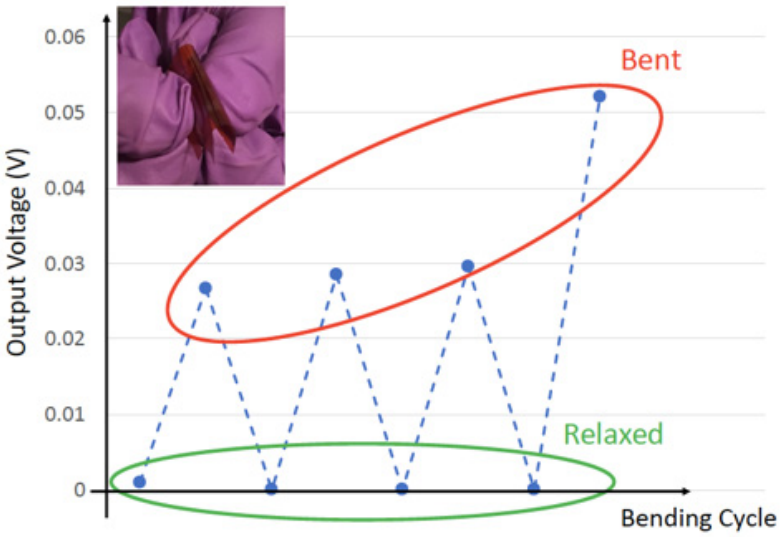

Figure 8. Bending experiment and the produced output voltage.

4.2. Mechanical and Electrical Measurements of GFRP

The stress–strain curves of GFRP composite coupons with and without 2.0 wt.% CNFs under static tension showed nonlinear behavior. It can also be observed that incorporating CNFs had no effect on the initial elastic modulus. The composite tension behavior is dominated by the matrix rather than the fibers due to the off-axis loading. Four distinct zones can be identified in the stress–strain curves, and are marked on the curves shown in Figure 9a.

At low stress (Zone 1), the contribution of glass fiber shall not be neglected. The relative high stiffness of glass fiber counteracts the effect of the CNFs. When the applied stress increases (Zone 2), the effect of CNFs on the composite behavior appears as interlaminar debonding, which occurs due to reduced fiber-matrix bond due to reduced crosslinking. This is reflected in Zone 2 and in the decreased stiffness of CNFs/GFRP coupons compared with GFRP composite with neat epoxy. At high applied stress levels (Zone 3), another effect of CNFs becomes apparent. Such softening in the polymer matrix limits its ability to restrain lateral fiber movement under tension loads, thus an apparent necking-like behavior takes place. This behavior is very pronounced with CNFs/GFRP coupons compared with GFRP coupons with neat epoxy. Such necking results in reduced cross-section and premature failure (Zone 4) at relatively lower elongation in CNFs/GFRP, compared with neat GFRP. Figure 9b shows damage propagation in GFRP composite coupons incorporating 2.0 wt.% CNFs under static tension.

A comparison between the damage metric observed using electrical conductivity monitoring and that quantified from the mechanical test using Equation (4) was made. It is apparent that incorporating CNFs at 2.0 wt.% loading enables a significant change in the electrical conductivity of GFRP relative to the ability to observe damage initiation and propagation with reasonable accuracy. Furthermore, both metrics increased gradually and reached a relatively flat plateau, showing constant damage in GFRP at the peak stress. The mechanical damage increase rate (damage propagation) is much faster compared with the electrical damage (see Figure 9b). The difference between the mechanical and electrical damage metrics can be explained by the difference in the significance of microcracks initiation and propagation on elastic modulus and electrical conductivity. While the elastic modulus is known to be significantly affected by cracking, the electrical conductivity might

not be influenced at the same rate if alternative electrically conductive paths can be found in the matrix. This means that using CNFs will improve GFRP conductivity, which makes it useful for electrical charge applications.

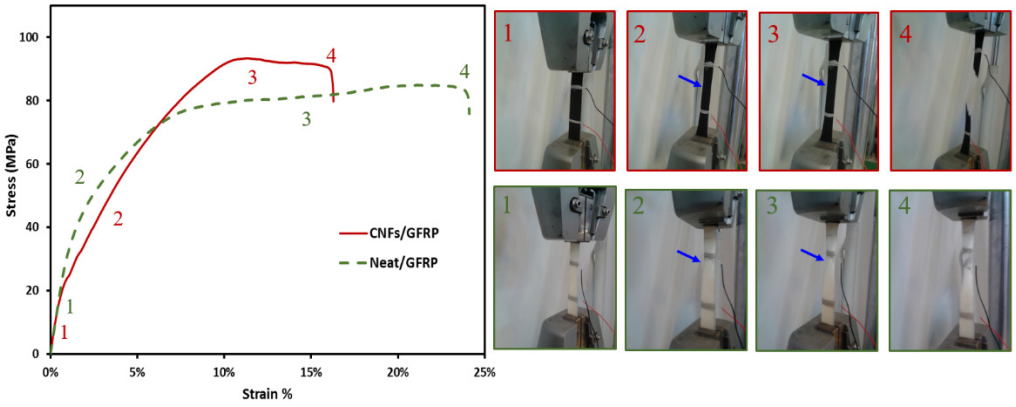

(**a**)

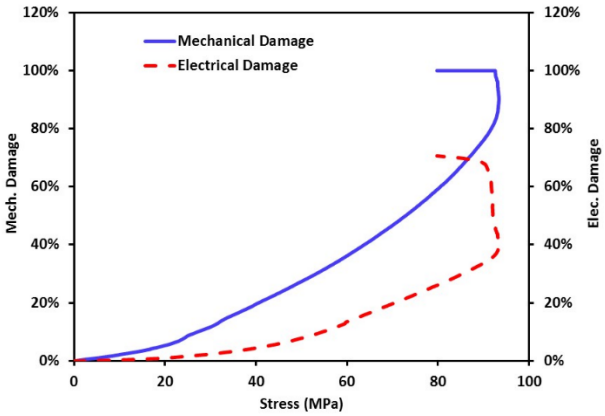

(**b**)

Figure 9. GFRP testing (**a**) Stress–strain curves of GFRP and electrically conductive GFRP incorporating 2.0% CNFs (**b**) stress-electrical damage (DE) and stress-mechanical damage (DM) for glass fiber composite incorporating CNFs under monotonically increasing static tension stress.

4.3. Test Results for the Lab-Scale Prototype

4.3.1. Stationary Tests Comparison of Indoors and Outdoors Settings

The output power from the three solar panels used in this study (as described in Section 3.1) is compared in indoor settings and artificial lights and outdoors with direct sunlight as shown in Figure 10. Due to the indoor settings and the plexiglass, the output of the solar panels is decreased by 25% from the maximum output that the panel can capture outdoors with direct sunlight.

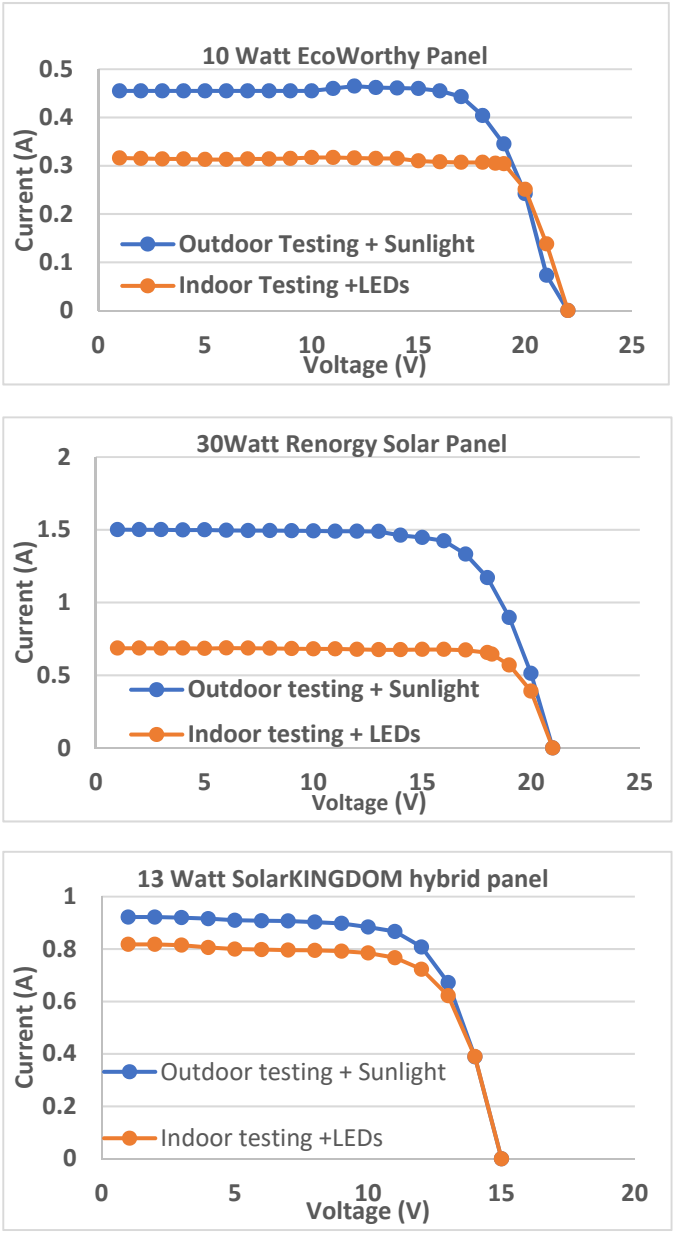

Figure 10. Testing the power output of the three solar panels used; outdoor with sunlight versus artificial light indoors.

4.3.2. Stationary Tests with Indoor Setting and Artificial LEDs

For the purpose of verifying the proposed concept of smart charging system, the LEDs were first powered using a DC power supply. The output power of the three solar panels in stationary without the plexiglass (163.6 lux output) and with plexiglass (120.1 lux output) were measured, and the results for the three solar panels under test are shown in Figure 11. The results show that the effect of the plexiglass is very minimal, which means that the transparent GFRP will not affect light output from the LEDs embedded in the roadway. However, it can be seen that the power output was about 62% of the rated power of the panels, and that is due to the LEDs. Further testing will compare the power output if the solar panels are tested outside and fed directly from the sun.

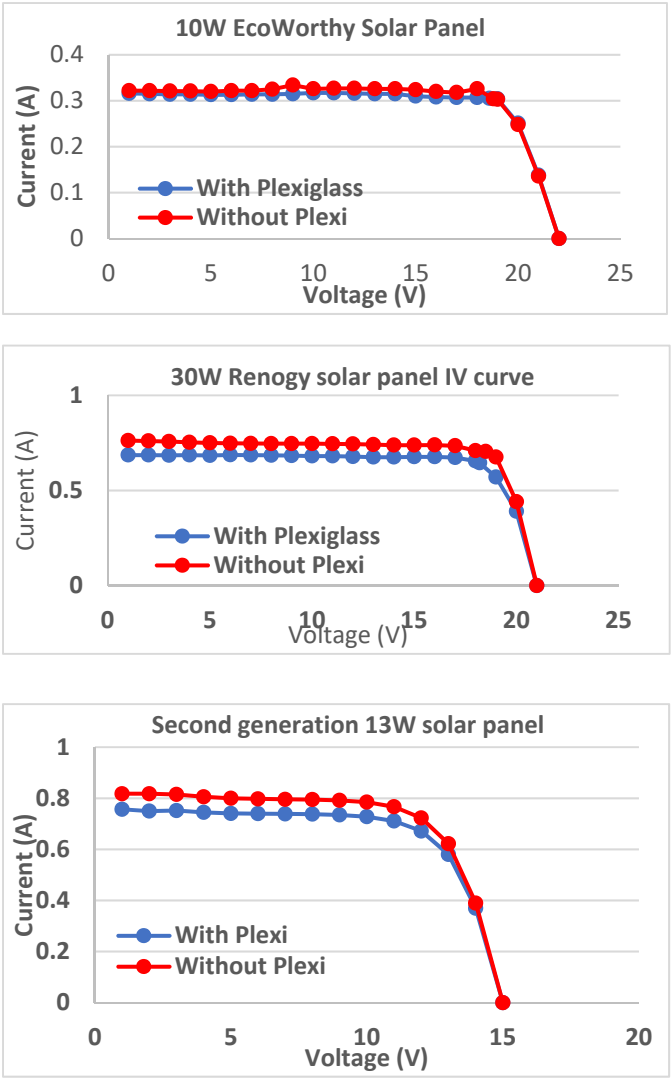

Figure 11. Testing the output power of the transparent plexiglass indoors with artificial light to determine the effects for the three solar panels.

4.3.3. Test of the Lab-Scale Prototype under Motion with Indoor Settings and Artificial LEDs

In this test, the three solar panel configurations depicted in Figure 7 were moved along the track with different velocities of 1.12 m/s, 2.24 m/s, and 3 m/s to simulate the vehicle with the solar panel on its bottom driven with different speeds, and with the load corresponding to the maximum output. The MPPT was calculated by sweeping a variable resistor and calculating the corresponding output power for each of the three solar panels under test, as shown in Figure 12. During stationary testing, all solar panels need different loads to achieve the MPPT point. The single 30 W panel, while being fully exposed to artificial light, was optimally loaded at 40 Ω, while the two 13 W panels performed best at 15 Ω, and the three 10 W panels performed best at 35 Ω.

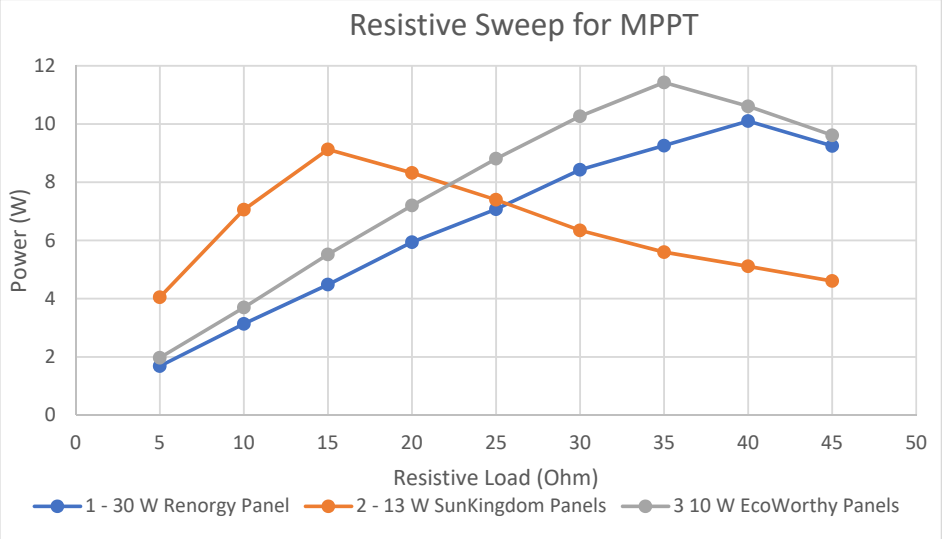

Figure 12. Sweeping resistive load to capture the maximum power output for one Renogy® 30 W panel, two of the13 W Sunkingdom® panel, and three of the 10 W EcoWorthy® panels.

Figures 13–15 depicts the output voltage, current, and power measured while the simulated vehicle is in motion. The maximum output power from the EcoWorthy® solar panel was 3.8 W from one panel, with a load of 40 Ω tracking the maximum power point. The prototype has three panels to cover all the LED area, and, therefore, the maximum output power for the prototype is 11.43 W. The three solar panels were replaced with one large solar panel (30 W Renogy®) and the output power was measured. Figure 13 shows a maximum power output of about 10.1 W. However, since the size of the panel is now covering most of the LED compartment, the solar panel will not have enough time to capture the energy from the LEDs. Therefore, it can be concluded that it is better to use smaller solar panels in parallel than one large solar panel. During the speed tests, it was concluded that at different speeds the output waveforms are approximately equivalent.

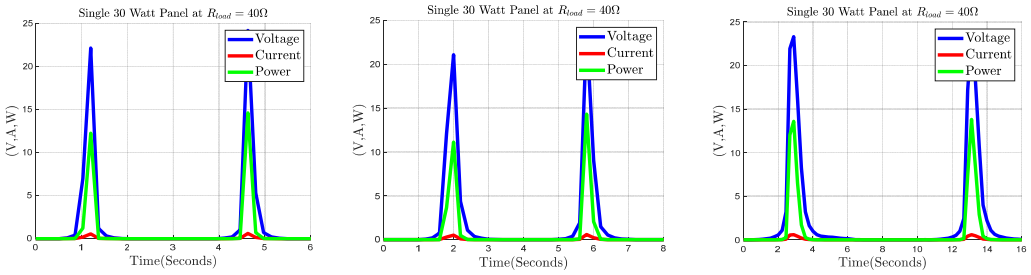

(**a**) (**b**) (**c**)

Figure 13. Output voltage, current, and power measured while simulated vehicle in motion using the 30 W Renogy® solar panel and under different speeds (1.12 m/s (**a**), 2.24 m/s (**b**) and 3 m/s (**c**), from left to right respectively).

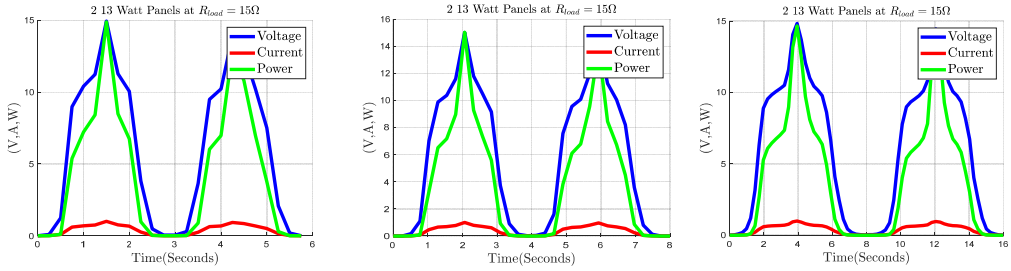

(**a**) (**b**) (**c**)

Figure 14. Output voltage, current, and power measured while simulated vehicle in motion using the 2 of 13 W SunKingdom® solar panels and under different speeds (1.12 m/s (**a**), 2.24 m/s (**b**), and 3 m/s (**c**), from left to right, respectively).

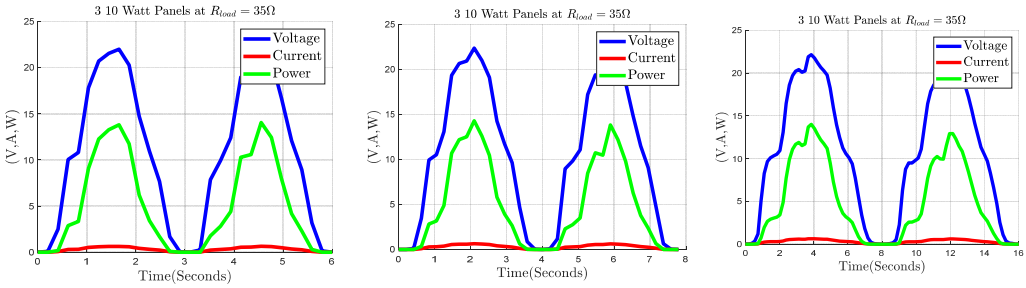

(**a**) (**b**) (**c**)

Figure 15. Output voltage, current and power measured while simulated vehicle in motion using the three 10 W EcoWorthy® solar panels and under different speeds (1.12 m/s (**a**), 2.24 m/s (**b**), and 3 m/s (**c**), from left to right, respectively).

For the EcoWorthy® configuration, the maximum power that can be delivered is 14.5 W (peak points), while, in motion, the average power delivered over time is approximately 4.9 W, meaning that the in motion the efficiency is 43%. For the SunKingdom® configuration, the maximum power delivered was 15 W, while, in motion, the average power delivered over time was approximately 4.1 W, meaning that the in motion the efficiency was 45%. For the Renogy® configuration the maximum power delivered was 14.8 W, while, in motion, the average power delivered over time was approximately one watt, meaning that, in motion, the efficiency is 10%. The results of the average power over time show that multiple smaller cells perform better than one single panel. This is due to others effects, such as shading.

5. Discussion: Recommended Strategy

5.1. System Embedded in Infrastructure

A standard lane is separated into five distinct pieces, the left edge, the left wheel path, the center zone, the right wheel path and the right edge. For this study, the right and left wheel paths are the focal points. In each respective wheel path, circuitry, materials, and polymers will be placed. Sawtooth cuts will be made in the wheel path, with the minimum width being 30 cm and the maximum being 107 cm. The minimum width is relative to the width of common tire sizes, such as the 225/65r17 tire that is 24 cm wide and the LT265/70R17 tire at 26 cm wide. The common tire widths and ample additions to both sides are the minimum width at 30 cm; this will work only if the EV is on a predetermined path and precisely controlled. Realistically, this will not be the case, and the cuts can be anywhere between the aforementioned range. The cuts will be made for both wheel paths (i.e., left and right).

An ideal cut would have the width of 45 cm and the length of 20 cm. The length of 20 cm is due to the approximate length of a vehicle. The length should be a minimum

of 182 cm due to the placement of the PV cells, which gives the full range of solar cells a chance to produce power at the same time. Moreover, only powering the lights that are directly under the solar cells is a key factor in increasing efficiency. An optimal way of lighting the LEDs should be researched. If the vehicles are automated and can travel the path at a predetermined speed, a simple lighting sequence can be implemented.

The recommended circuitry that will be embedded in the cuts are broken up into four parts, the nanomaterial and the output voltage, a full-bridge rectifier, a fly-back converter, and LED strips. The nanomaterial output voltage is a sinusoidal wave generated from the scaled up MoS_2 that generates electricity from mechanical pressure or heat. That waveform will then be rectified going through the full bridge rectifier. The waveform is rectified so that there is no negative current to control in the circuitry going forward. The rectified waveform is used as the input to a fly-back converter and controlled though a constant voltage controller to control the output to approximately 22 V, the operating voltage of the LEDs. The reason a fly-back converter is being used is due to the expected large magnitude of the rectified signal. From piezoelectric materials, one can expect high voltages with extremely low current. This is where the fly-back converter can regulate the voltage and give a usable current to power the final stage, the LEDs. The LEDs are the output on the embedded roadway circuitry, and the input to the EV circuitry system, described in the next section.

For the cuts that will be made, approximately 32, 1220 mm $\times$ 18 mm Samsung Semiconductor Inc. (San Jose, CA, USA) LT-Qxx2A series LED module strips will be embedded into each wheel path cut. This will allow for adequate room for the LED strips along with room for the illumination to be taken advantage of.

5.2. System for EVs

A PV array will be placed on the underside of an EV to capture the illumination from the LEDs embedded in the roadway, as discussed in the above section. The PV array will exist between the wheel wells of each respective side (i.e., left and right). This means that the PV array will run along the rocker panels of the vehicles, which are approximately six feet in length. For these dimensions we can fit 24 solar cells, as PV cells come in a standard size of $6'$ by $6'$. The array will consist of 24 solar cells in parallel, placed in 2×12 cells. This means that the voltage will stay in the range of 0–24 V, and the current will be cascaded. With the solar cells in this configuration, shading plays a less pivotal role. These are approximate measures due to vehicles differing in dimensions. To capture and deliver the power, the group is proposing the three stages: the PV cells in parallel as discussed, a buck-boost converter, and then the battery of the proposed EV. The output of the solar cells should be in parallel with a load capacitor to smooth the voltage that will act as the input for a buck-boost converter. The proposed buck-boost converter is used to regulate the voltage to 12 V to be fed into the final stage, the EVs battery. The power fed into the battery will help add slow charging over time while the EV is in motion.

6. Conclusions and Future Work

This study presented an innovative smart illuminative charging system for EVs. It is a novel (because it is induction coil-free) wireless charging mechanism that uses nanomaterials-powered LEDs embedded within the road pavement and thin film solar panels placed on the bottom of the EVs to charge the vehicle battery. Light mediates energy transfer between LEDs and solar panels. To better protect the LEDs from the heavy vehicle load whilst still harnessing their electric-to-optical energy conversion capability, certain flexible polymer overlay materials were developed to be placed onto the pavement surface. The study presented the initial, albeit promising, results on the great potential of the nanomaterials to harvest energy and provide electricity to light up the LEDs. However, one of the challenges in implementation is to fabricate EH2N in a large scale to be used commercially. For future work, the authors are also investigating other piezoelectric materials that are commercially available to operate with the same concept. A GFRP was fabricated as an

overlay for the nanomaterials for the roadway compartments and tested for mechanical stress to ensure the performance of load testing of the vehicle and electrical conductivity.

A lab-scale proof-of-concept prototype was also demonstrated to verify the system-level capability. Different solar panels were tested, and it was concluded that the solar panel size should be smaller than the LED compartments embedded in the roadways for best results. In addition, it was shown that the best results came from the solar panel that combines the first- and second-generation panel characteristics, thus simultaneously mono-crystalline and flexible. It was shown that the start-to-end energy efficiency was about 40%. A strategy for implementation was proposed for both the embedded roadway and the circuits for the EV. Dimensions of the compartments and the contents of the compartments were discussed, as well as the configuration of the solar panels and power stage to charge the battery.

If this clean, wireless charging method for EVs is adapted, it will lead to a significant decrease in CO_2 emissions. Comparing with gas-powered vehicles, the CO_2 emission is decreased 50% in EVs, from 57 to 28 metric tons. This will help reduce the impact of climate change on the reliability and capacity of transportation systems. In addition, with the energy harvested from the pavement using these nanomaterials, the system can also be used as a sensor for vehicle counts and traffic data collection. This sensing technology can help improve safety and reduce congestion.

Author Contributions: Conceptualization, S.A., E.C.A., M.M.R.T. and S.D.; methodology, D.F., A.S., P.R., and M.G.; software, D.F., A.S., P.R. and M.G.; formal analysis, D.F., A.S., P.R. and M.G. All authors have read and agreed to the published version of the manuscript.

Funding: This research was funded by Transportation Consortium of South-Central States (Tran-SET) University Transportation Center, grant number 18ITSTSA03.

Data Availability Statement: The data presented in this study are available on request from the corresponding author.

Acknowledgments: This work is part of a project funded by the Transportation Consortium of South-Central States (Tran-SET) University Transportation Center (Project No. 18ITSTSA03).

Conflicts of Interest: The authors declare no conflict of interest.

References

1. Dept. of Transportation. *Sustainability in Roadway Design and Construction Guidance Document*; CDOT Environmental Programs Branch: Denver, CO, USA, 2013.
2. Newman, P.; Hargroves, K.; Desha, C.; Whistler, L.; Farr, A.; Wilson, K.; Beauson, J.; Matan, A.; Surawski, L. Reducing the Environmental Impact of Road Construction. 2012. Available online: https://sbenrc.com.au/app/uploads/2013/11/SBEnrc-Project-1.3-Briefing-Report-Reducing-energy-intensity-of-road-construction.pdf (accessed on 3 January 2021).
3. Konstantinou, T.; Gkartzonikas, C.; Gkritza, K. Public acceptance of electric roadways: The case of Los Angeles, California. *Int. J. Sustain. Transp.* **2021**, *22*, 1–25. [CrossRef]
4. US. *Environmental Protection Agency. Global, Regional, and National Fossil-Fuel CO2 Emissions*; EPA: Washington, DC, USA, 2017.
5. Moon, H.; Youngjun Park, S.; Jeong, C.; Lee, J. Forecasting electricity demand of electric vehicles by analyzing consumers' charging patterns. *Transp. Res. Part D Transp. Environ.* **2018**, *62*, 64–79, ISSN 1361–9209. [CrossRef]
6. Shepero, M. Modeling and Forecasting of Electric Vehicle Charging, Solar Power Production, and Residential Load: Perspectives into the Future Urban and Rural Energy Systems. Ph.D. Dissertation, Uppsala University, Disciplinary Domain of Science and Technology, Technology, Department of Civil and Industrial Engineering, Civil Engineering and Built Environment, Uppsala, Sweden, 2020. Available online: http://urn.kb.se/resolve?urn=urn:nbn:se:uu:diva-416754 (accessed on 3 January 2021).
7. Gerossier, A.; Girard, R.; Kariniotakis, G. Modeling and Forecasting Electric Vehicle Consumption Profiles. *Energies* **2019**, *12*, 1341. [CrossRef]
8. Konstantelos, I.; Giannelos, S.; Strbac, G. Strategic Valuation of Smart Grid Technology Options in Distribution Networks. *IEEE Trans. Power Syst.* **2017**, *32*, 1293–1303. [CrossRef]
9. van der Weijde, A.; Hobbs, B. Planning electricity transmission to accommodate renewables: Using two-stage programming to evaluate flexibility and the cost of disregarding uncertainty. *Energy Econ.* **2012**, *34*, 2089–2101. [CrossRef]
10. Taljegard, M.; Göransson, L.; Odenberger, M.; Johnsson, F. Impacts of electric vehicles on the electricity generation portfolio–A Scandinavian-German case study. *Appl. Energy* **2019**, *235*, 1637–1650. Available online: http://www.sciencedirect.com/science/article/pii/S0306261918316970 (accessed on 4 January 2021). [CrossRef]

11. Borozan, S.; Giannelos, S.; Strbac, G. Strategic network expansion planning with electric vehicle smart charging concepts as investment options. *Adv. Appl. Energy* **2022**, *5*, 100077, ISSN 2666-7924. [CrossRef]
12. Trieu, M.; Jadun, P.; Logan, J.; McMillan, C.; Muratori, M.; Steinberg, D.; Vimmerstedt, L.; Jones, R.; Haley, B.; Nelson, B. *Electrification Futures Study: Scenarios of Electric Technology Adoption and Power Consumption for the United States*; National Renewable Energy Laboratory: Golden, CO, USA, 2018; NREL/TP-6A20–71500. Available online: https://www.nrel.gov/docs/fy18osti/71500.pdf (accessed on 4 January 2021).
13. Yuksel, T.; Michalek, J.J. Effects of Regional Temperature on Electric Vehicle Efficiency, Range, and Emissions in the United States. *Environ. Sci. Technol.* **2015**, *49*, 3974–3980. [CrossRef]
14. Gerssen-Gondelach, S.; Faaij, A. Performance of batteries for electric vehicles on short and longer term. *J. Power Sources* **2012**, *212*, 111. [CrossRef]
15. Etacheri, V.; Marom, R.; Elazari Salitra, R.; Aurbach, D. Challenges in the development of advanced Li-ion batteries: A review. *Energy Environ. Sci.* **2011**, *4*, 3243. [CrossRef]
16. Zhou, Y.; Gohlke, D.; Rush, L.; Kelly, J.; Dai, Q. *Lithium-Ion Battery Supply Chain for E-Drive Vehicles in the United States: 2010–2020*; Argonne National Lab: Lemont, IL, USA, 2021.
17. Ahmed, S.; Bloom, I.; Jansen, A.N.; Tanim, T.; Dufek, E.J.; Pesaran, A.; Burnham, A.; Cason, R.B.; Dias, F.; Hardy, K.; et al. Enabling fast charging–A battery technology gap assessment. *J. Power Sources* **2017**, *367*, 250–262, ISSN 0378–7753. [CrossRef]
18. Mastoi, M.S.; Zhuang, S.; Munir, H.M.; Haris, M.; Hassan, M.; Usman, M.; Bukhari, S.S.H.; Ro, J.-S. An in-depth analysis of electric vehicle charging station infrastructure, policy implications, and future trends. *Energy Rep.* **2022**, *8*, 11504–11529, ISSN 2352–4847. [CrossRef]
19. Li, S.; Mi, C.C. Wireless Power Transfer for Electric Vehicle Applications. *IEEE J. Emerg. Sel. Top. Power Electron.* **2015**, *3*, 4–17. [CrossRef]
20. Will Electric Cars soon Have Solar Roofs? *Toyota and Tesla Say Yes, ThinkProgress.org*. Available online: https://thinkprogress.org/prius-solar-roof-breakthrough-2b929f467061/ (accessed on 9 March 2018).
21. André, K.; Aristeidis, K.; Robert, M.; Joannopoulos, J.D.; Peter, F.; Marin, S. Wireless Power Transfer via Strongly Coupled Magnetic Resonances. *J. Sci. P* **2007**, *317*, 83–86. [CrossRef]
22. Sample, A.; Meyer, D.; Smith, J. Analysis, experimental results, and range adaptation of magnetically coupled resonators for wireless power transfer. *IEEE Trans. Ind. Electron.* **2011**, *58*, 544–554. [CrossRef]
23. Cannon, B.; Hoburg, J.; Stancil, D.; Goldstein, S. Magnetic resonant coupling as a potential means for wireless power transfer to multiple small receivers. *IEEE Trans. Power Electron.* **2009**, *24*, 1819–1825. [CrossRef]
24. Kurs, A.; Moffatt, R.; Soljacic, M. Simultaneous mid-range power transfer to multiple devices. *Appl. Phys. Lett.* **2010**, *96*, 044102-1–044102-3. [CrossRef]
25. Cheon, S.; Kim, Y.-H.; Kang, S.-Y.; Lee, M.L.; Lee, J.-M.; Zyung, T. Circuit-Model-Based Analysis of a Wireless Energy-Transfer System via Coupled Magnetic Resonances. *IEEE Trans. Ind. Electron.* **2011**, *58*, 2906–2914. [CrossRef]
26. Chen, K.; Zhao, Z. Analysis of the Double-Layer Printed Spiral Coil for Wireless Power Transfer. *IEEE J. Emerg. Sel. Top. Power Electron.* **2013**, *1*, 114–121. [CrossRef]
27. Zhang, Y.; Zhao, Z.; Chen, K. Frequency Decrease Analysis of Resonant Wireless Power Transfer. *IEEE Trans. Power Electron.* **2014**, *29*, 1058–1063. [CrossRef]
28. Nagatsuka, Y.; Ehara, N.; Kaneko, Y.; Abe, S.; Yasuda, T. Compact contactless power transfer system for electric vehicles. In Proceedings of the 2010 International Power Electronics Conference-ECCE ASIA, Sapporo, Japan, 21–24 June 2010; pp. 807–813. [CrossRef]
29. Lee, S.; Huh, J.; Park, C.; Choi, N.S.; Cho, G.H.; Rim, C.T. On-Line Electric Vehicle using inductive power transfer system. In Proceedings of the 2010 IEEE Energy Conversion Congress and Exposition, Atlanta, GA, USA, 12–16 September 2010; pp. 1598–1601. [CrossRef]
30. Huh, J.; Lee, W.; Cho, G.H.; Lee, B.; Rim, C.T. Characterization of novel Inductive Power Transfer Systems for On-Line Electric Vehicles. In Proceedings of the 2011 Twenty-Sixth Annual IEEE Applied Power Electronics Conference and Exposition (APEC), Fort Worth, TX, USA, 6–11 March 2011; pp. 1975–1979. [CrossRef]
31. Ning, P.; Miller, J.M.; Onar, O.C.; White, C.P.; Marlino, L.D. A compact wireless charging system development. In Proceedings of the 2013 Twenty-Eighth Annual IEEE Applied Power Electronics Conference and Exposition (APEC), Long Beach, CA, USA, 17–21 March 2013; pp. 3045–3050. [CrossRef]
32. Nguyen, T.D.; Li, S.; Li, W.; Mi, C.C. Feasibility study on bipolar pads for efficient wireless power chargers. In Proceedings of the 2014 IEEE Applied Power Electronics Conference and Exposition-APEC 2014, Fort Worth, TX, USA, 16–20 March 2014; pp. 1676–1682. [CrossRef]
33. Caughill, P. This High-Tech, Solar-Powered Car May be the Ruture of Travel. 2017. Available online: https://futurism.com/this-futuristic-solar-powered-car-may-be-the-future-of-travel/ (accessed on 22 March 2018).
34. Lufčić, M.; Maras, M.; Vukelić, M. Energy saving design and materials in road transport. In Proceedings of the REACT Conference, Beograd, Serbia, 3–4 May 2011. Available online: http://bib.irb.hr/prikazi-rad?rad=540022 (accessed on 20 March 2018).
35. Ranjan, R. Solar Power Roads: Revitalising Solar Highways, Electrical Power and Smart Grids. *Int. J. Eng. Res. Gen. Sci.* **2015**, *3*, 380–385.

36. Bobes-Jesus, V.; Pascual-Munoz, P.; Castro-Fresno, D.; Rodriguez-Hernandez, J. Asphalt solar collectors: A literature review. *Appl. Energy* **2013**, *102*, 962–970. [CrossRef]
37. Larsson, O.; Thelandersson, S. Estimating extreme values of thermal gradients in concrete structures. *Mater. Struct.* **2011**, *44*, 1491–1500. [CrossRef]
38. Navarro, G.; Rojas, C. Piezoelectric Power Generating Tire Apparatus. U.S. Patent US20170084817A1, 23 March 2017.
39. Kumar, A.; Sumathi, S. Renewable energy source piezo electric harvesters in car tyres. In Proceedings of the 2015 Online International Conference on Green Engineering and Technologies, Coimbatore, India, 27 November 2015.
40. Allouhi, A.; Rehman, S.; Buker, M.S.; Said, Z. Up-to-date literature review on Solar PV systems: Technology progress, market status and R&D. *J. Clean. Prod.* **2022**, *362*, 132339. [CrossRef]
41. Benda, V.; Černá, L. PV cells and modules–State of the art, limits and trends. *Heliyon* **2020**, *6*, e05666. [CrossRef]
42. Babics, M.; De Bastiani, M.; Balawi, A.H.; Ugur, E.; Aydin, E.; Subbiah, A.S.; Liu, J.; Xu, L.; Azmi, R.; Allen, T.G.; et al. Unleashing the Full Power of Perovskite/Silicon Tandem Modules with Solar Trackers. *ACS Energy Lett.* **2022**, *7*, 1604–1610. [CrossRef]
43. Lee, K.; Um, H.-D.; Choi, D.; Park, J.; Kim, N.; Kim, H.; Seo, K. The Development of Transparent Photovoltaics. *Cell Rep. Phys. Sci.* **2020**, *1*, 100143. [CrossRef]
44. Solid-State Lighting: Comparing LEDs to Traditional Light Sources. Available online: https://www.eere.energy.gov (accessed on 22 March 2018).
45. *Lifetime of White LEDs*; US Department of Energy: Washington, DC, USA, 2012.
46. Wang, F.-K.; Lu, Y.-C. Useful lifetime analysis for high-power white LEDs. *Microelectron. Reliab.* **2014**, *54*, 1307–1315. [CrossRef]
47. In Depth: Advantages of LED Lighting. Available online: https://www.energy.ltgovernors.com (accessed on 22 March 2018).
48. Available online: https://www.samsung.com/led/lighting/mid-power-leds/5630-leds/lm561c/# (accessed on 24 December 2022).
49. Anton, S.; Erturk, E.; Kong, N.; Ha, D.; Inman, D. Self-charging structures using piezoceramics and thin-film batteries. In Proceedings of the ASME Conf. Smart Mater., Adaptive Struct. Intell. Syst., Oxnard, CA, USA, 21–23 September 2009; pp. 1–11.
50. Wu, W.; Wang, L.; Li, Y.; Zhang, F.; Lin, L.; Niu, S.; Chenet, D.; Zhang, X.; Hao, Y.; Heinz, T.F.; et al. Piezoelectricity of single-atomic-layer MoS2 for energy conversion and piezotronics. *Nature* **2014**, *514*, 470. [CrossRef] [PubMed]
51. Zhu, H.; Wang, Y.; Xiao, J.; Liu, M.; Xiong, S.; Wong, Z.J.; Ye, Z.; Ye, Y.; Yin, X.; Zhang, X. Observation of piezoelectricity in free-standing monolayer MoS2. *Nat. Nanotechnol.* **2015**, *10*, 151. [CrossRef]
52. Buscema, M.; Barkelid, M.; Zwiller, V.; van der Zant, H.S.J.; Steele, G.A.; Castellanos-Gomez, A. Large and Tunable Photothermoelectric Effect in Single-Layer MoS_2. *Nano Lett.* **2013**, *13*, 358–363. [CrossRef] [PubMed]
53. Ferrari, A.C.; Meyer, J.C.; Scardaci, V.; Casiraghi, C.; Lazzeri, M.; Mauri, F.; Piscanec, S.; Jiang, D.; Novoselov, K.S.; Roth, S.; et al. Raman Spectrum of Graphene and Graphene Layers. *Phys. Rev. Lett.* **2006**, *97*, 187401. [CrossRef] [PubMed]
54. US Composites. Epoxy Resins. Available online: https://www.uscomposites.com/products.html (accessed on 14 December 2022).
55. ACP Composites. Available online: https://www.acpcomposites.com/ (accessed on 14 December 2022).
56. Large Scale Testing. MTS Machine. Available online: http://taha.unm.edu/research-2/large-scale-testing/ (accessed on 14 December 2022).
57. Sharma, C.; Jain, A. Maximum Power Point Tracking Techniques: A Review. *Int. J. Recent Res. Electr. Electron. Eng. (IJRREEE)* **2014**, *1*, 25–33.
58. Texas Instruments bq24800EVM Controller Evaluation Module (EVM). Available online: https://www.mouser.com/new/texas-instruments/ti-bq24800evm-evaluation-module/?gclid=Cj0KCQiAqOucBhDrARIsAPCQL1azXxb4u4TLWfXbhWx6ZCgRUkclK6akYwdhBbbbP9mFyQpdkneMLwoaApBCEALw_wcB (accessed on 14 December 2022).
59. HC-05 Bluetooth Module. Available online: https://www.electronicwings.com/sensors-modules/bluetooth-module-hc-05- (accessed on 14 December 2022).
60. Matlab Mathworks. Available online: https://www.mathworks.com/products/matlab.html (accessed on 14 December 2022).